catalysts

MDPI

Article

Fabrication of Hierarchically Porous Reduced Graphene Oxide/$SnIn_4S_8$ Composites by a Low-Temperature Co-Precipitation Strategy and Their Excellent Visible-Light Photocatalytic Mineralization Performance

Fang Deng [1], Xule Pei [1], Yiting Luo [1], Xubiao Luo [1,*], Dionysios D. Dionysiou [2], Shaolin Wu [1] and Shenglian Luo [1,*]

[1] Key Laboratory of Jiangxi Province for Persistent Pollutants Control and Resources Recycle, Nanchang Hangkong University, Nanchang 330063, China; 40030@nchu.edu.cn (F.D.); pxl041256@126.com (X.P.); 70240@nchu.edu.cn (Y.L.); 39008@nchu.edu.cn (S.W.)

[2] Department of Biomedical, Chemical and Environmental Engineering (DBCEE), University of Cincinnati, Cincinnati, OH 45221-0012, USA; dionysios.d.dionysiou@uc.edu

* Correspondence: 40029@nchu.edu.cn (X.L.); sllou@hnu.edu.cn (S.L.); Tel.: +86-791-8395-3372 (X.L.); +86-791-8386-3688 (S.L.); Fax: +86-791-8395-373 (X.L.); +86-791-8386-3688 (S.L.)

Academic Editor: Keith Hohn
Received: 11 June 2016; Accepted: 12 July 2016; Published: 29 July 2016

Abstract: Hierarchically porous reduced graphene oxide/$SnIn_4S_8$ (RGO/$SnIn_4S_8$) composites with visible-light response and strong mineralization ability were first successfully prepared by a facile low-temperature co-precipitation method, and were characterized by X ray diffraction (XRD), scanning electron microscope (SEM), Brunauer-Emmet-Teller (BET), UV-Visible spectrophotometer (UV-Vis), Raman spectra and Photoluminescence (PL) techniques. RGO/$SnIn_4S_8$ composite exhibits strong absorption in UV and visible-light range. The optimized 5% RGO/$SnIn_4S_8$ possesses the optimal photocatalytic degradation efficiency and the best mineralization performance with complete degradation of Rhodamine B (RhB) within 70 min and 73.17% mineralization yield within 160 min under visible-light irradiation, which is much higher than that of pure $SnIn_4S_8$. The main reactive species, which play crucial roles in the degradation and mineralization of RhB, follow the order of $h^+ > \cdot O_2^- > \cdot OH$. The intermediate products of RhB degradation were analyzed by using high performance liquid chromatography-tandem mass spectrometry (HPLC-MS), and the possible degradation pathways and mechanism were proposed. Moreover, 5% RGO/$SnIn_4S_8$ exhibits excellent reusability and stability without an obvious decrease in photocatalytic activity after four consecutive photocatalytic degradation-regeneration experiments.

Keywords: $SnIn_4S_8$; reduced graphene oxide; composite; visible light; mineralization

1. Introduction

Water pollution has attracted public attention due to the environmental and health risks [1–5]. Dye contamination has become a major factor that contributes to water quality deterioration, and poses a potential hazard to living organisms due to the toxic, carcinogenic and mutagenic properties of dyes and their by-products [6–10]. Hence, the removal of organic dye pollutants from the wastewater becomes very essential. Up to now, several methods have been adopted to remove dyes from wastewater, including adsorption, coagulation, biological treatment, electrochemical treatment and heterogeneous photocatalytic oxidation technology [11–15]. Among these methods, heterogeneous photocatalytic oxidation technology is one of the best available technologies for dye removal from

wastewater due to its strong oxidation power, moderate operation temperature, and green-chemistry related procedures.

To date, TiO_2 is regarded as one of the most promising semiconductor photocatalysts for degrading organic compounds because of its high photocatalytic activity, low cost, non-toxicity, chemical stability, and biocompatibility [16–19]. However, TiO_2 has a large band gap (3.2 eV for anatase and 3.0 eV for rutile) and can only respond to ultraviolet (UV) irradiation, which restrict its practical application [20–23]. Moreover, a number of intermediates are usually produced during the TiO_2 photocatalytic degradation process, and are difficult to be further degraded. Some intermediates are even more toxic than their parental pollutants, thus it is urgent to develop new visible-light-responsive photocatalysts that can mineralize pollutants to inorganic products within a short reaction time.

Ternary chalcogenide compounds have attracted much concern due to their narrow band gap and high stability. Stannum indium sulfide ($SnIn_4S_8$) is a representative ternary chalcogenide semiconductor, and exhibits potential application in photocatalysis [24–26]. However, a single $SnIn_4S_8$ semiconductor usually has a small specific surface area and fast electron–hole recombination, which limit its photocatalytic efficiency. Hence, further modification of $SnIn_4S_8$ photocatalysts for high photon quantum efficiency is indispensable.

Reduced graphene oxide (RGO) has large specific surface area, superior electrical conductivity, high carrier mobility, and excellent mechanical properties, and is usually used as a good support to enhance the photocatalytic activities of some photocatalysts [27–31]. Herein, we first report a facile and simple synthesis of reduced graphene oxide/$SnIn_4S_8$ (RGO/$SnIn_4S_8$) composites with strong mineralization ability by a low-temperature co-precipitation method. The morphology, structure and photocatalytic activity of the RGO/$SnIn_4S_8$ composites were studied. The photocatalytic degradation kinetics, mineralization kinetics and degradation pathways of Rhodamine B (RhB) were systematically investigated under visible-light irradiation. Moreover, the possible photocatalytic mechanism of RGO/$SnIn_4S_8$ was provided.

2. Results and Discussion

2.1. Morphology Analysis

SEM images of RGO, pure $SnIn_4S_8$ and RGO/$SnIn_4S_8$ composite are shown in Figure 1. As shown in Figure 1a, the bare RGO is full of wrinkles, and the wrinkles form a curled and corrugated morphology. Pure $SnIn_4S_8$ possesses a network-like superstructure, which is constructed by numerous two-dimensional (2D) nanosheets with a thickness of about 10 nm. The assembly of the nanosheets produces abundant hierarchical pores at nanoscale (Figure 1b). In the case of the RGO/$SnIn_4S_8$ composite (Figure 1c), the nanosheets become obviously thinner, and the hierarchical pores between the nanosheets are smaller than those of pure $SnIn_4S_8$.

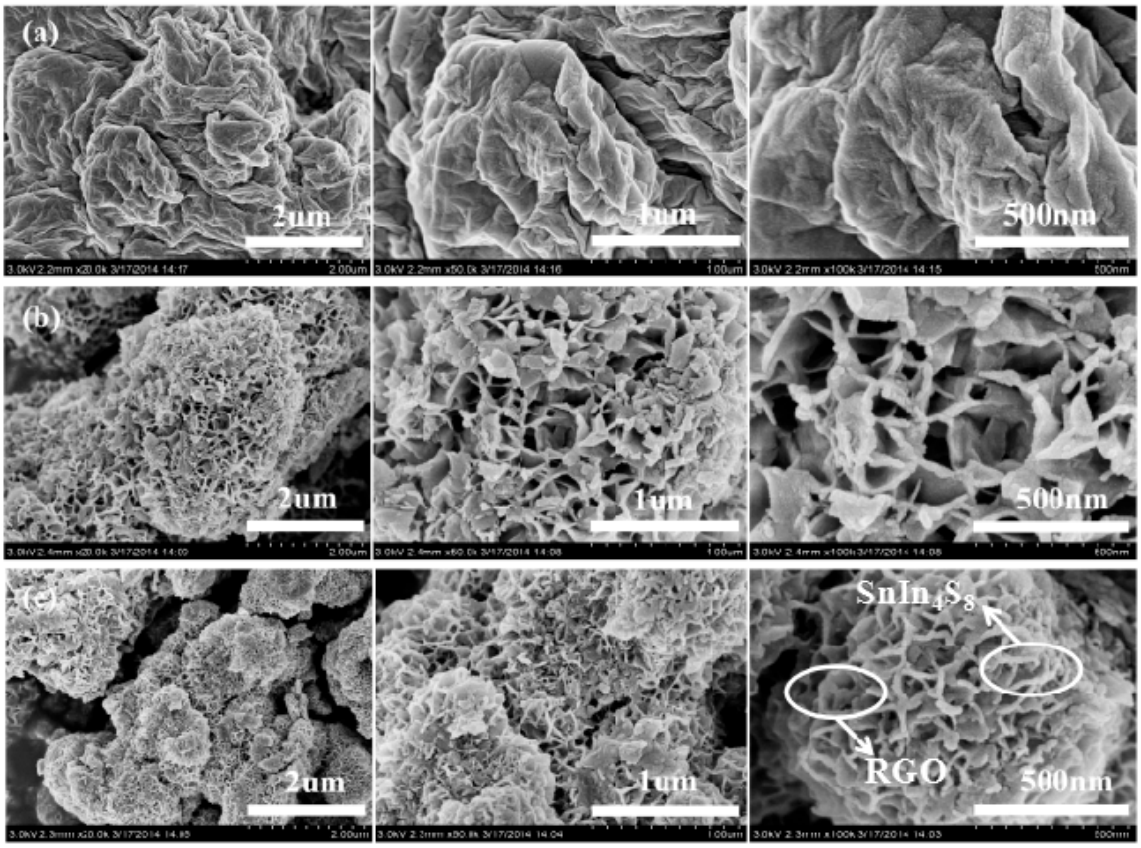

Figure 1. Scanning electron microscope (SEM) images of (**a**) reduced graphene oxide (RGO); (**b**) pure $SnIn_4S_8$ and (**c**) RGO/$SnIn_4S_8$ composite.

2.2. XRD Analysis

Figure 2 shows the XRD patterns of bare RGO, pure $SnIn_4S_8$ and RGO/$SnIn_4S_8$ composite. It is obvious that bare RGO shows two characteristic diffraction peaks at 22.9° and 42.7°, corresponding to (002) and (100) planes of RGO [32]. The pure $SnIn_4S_8$ and RGO/$SnIn_4S_8$ composite have similar XRD profiles. The main diffraction peaks are observed at about 2θ = 19.0°, 28.4° and 50.1°, which can be indexed to the (202), (600) and (001) crystalline planes of tetragonal phase of $SnIn_4S_8$, respectively [33]. However, no RGO characteristic diffraction peaks are found in the XRD patterns of RGO/$SnIn_4S_8$ composite, which is possibly due to the limited amount and the destroyed regular stacks of RGO in the composite [34].

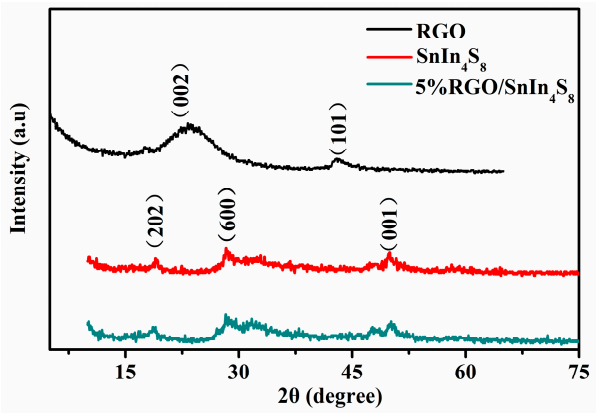

Figure 2. X ray diffraction (XRD) patterns of RGO, pure $SnIn_4S_8$, and RGO/$SnIn_4S_8$ composite.

2.3. Raman Spectroscopy

It is well known that Raman spectroscopy is a powerful method for the characterization of sp^2 and sp^3 hybridized carbon atoms in graphene to distinguish the ordered and disordered/defect structures. Therefore, Raman spectroscopy of GO, RGO, $SnIn_4S_8$ and RGO/$SnIn_4S_8$ composite was carried out (Figure 3). The two characteristic peaks of GO can be found at 1350 and 1585 cm^{-1}, corresponding to the D band (disorder peak) and G band (graphitic peak), respectively. The D band and G band of RGO located at 1344 and 1599 cm^{-1}, respectively. The shift of D band to around 1344 cm^{-1} indicates the considerable increase in thickness of graphitic structure and size of the in-plane sp^2 domains [35]. In case of $SnIn_4S_8$, $SnIn_4S_8$ shows strong Raman characteristic peaks at 323 cm^{-1}. For the RGO/$SnIn_4S_8$ composite, we observed the characteristic bands of $SnIn_4S_8$ at 323 cm^{-1} as well as the D band (ca. 1329 cm^{-1}) and G band (ca. 1602 cm^{-1}) of RGO, suggesting that the structure of RGO is maintained in the RGO/$SnIn_4S_8$ composite. The intensity ratio of D band to G band (I_D/I_G) can estimate the degree of disorder/defects in graphene. The I_D/I_G of GO is about 0.945, while the I_D/I_G of RGO and RGO/$SnIn_4S_8$ composite is about 1.118 and 1.146, respectively. The increase of I_D/I_G is attributed to the reduction and restoration of the sp^2 network of GO during the reduction process and the formation of more defects in RGO.

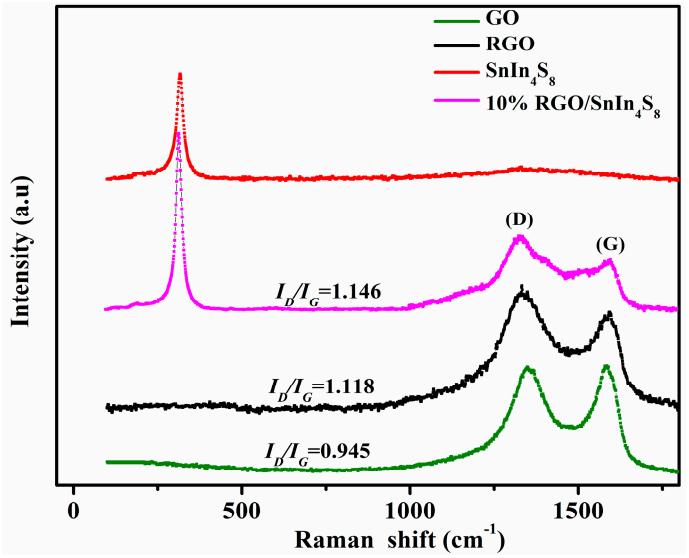

Figure 3. Raman spectroscopy of GO, RGO, pure $SnIn_4S_8$, and RGO/$SnIn_4S_8$ composite.

2.4. BET Surface Areas and Pore Structures

The Brunauer-Emmet-Teller (BET) surface area and pore structure play important roles in the photocatalytic performance of photocatalysts. Figure 4 shows the nitrogen adsorption-desorption isotherms and the corresponding pore size distribution curves of RGO, pure $SnIn_4S_8$ and RGO/$SnIn_4S_8$ composites with different RGO content. The nitrogen adsorption-desorption curves of these samples are type IV (Brunauer-Deming-Deming-Teller (BDDT) classification), indicating the presence of mesopores [36]. These isotherms exhibit H_3 hysteresis loops, suggesting that slit-like pores were formed by the aggregation of plate-like particles, which is consistent with the above SEM analysis. The results of BET surface area, pore volume, and average pore size of RGO, pure $SnIn_4S_8$ and RGO/$SnIn_4S_8$ are listed in Table 1. With the increase of RGO content in the composite samples, the specific surface area increases first and then decreases. When the content of RGO is 1% and 5%, the specific surface area is the largest (about 35 $m^2 \cdot g^{-1}$) [37–39].

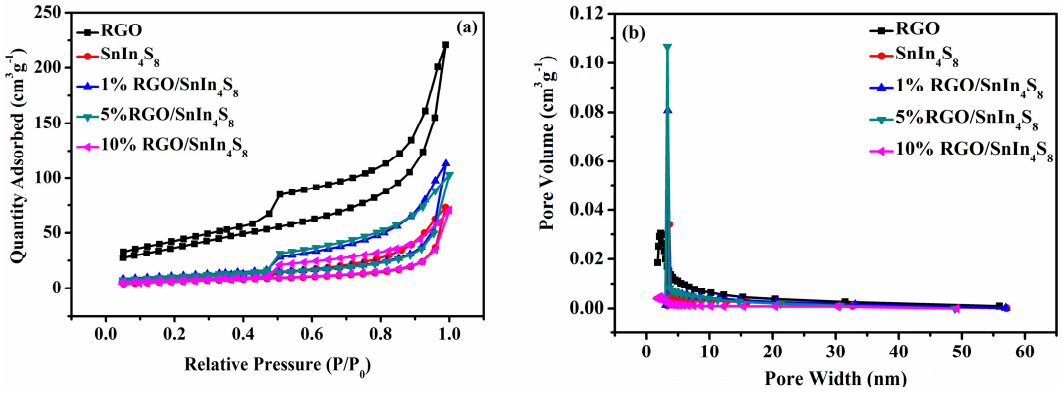

Figure 4. Nitrogen adsorption-desorption isotherms (**a**) and the corresponding pore size distribution curves (**b**) of RGO, pure $SnIn_4S_8$, and RGO/$SnIn_4S_8$ composites with different RGO content.

Table 1. Physical properties of reduced graphene oxide (RGO), pure $SnIn_4S_8$ and RGO/$SnIn_4S_8$ composites with different RGO content.

Samples	S_{BET} ($m^2 \cdot g^{-1}$)	Pore Volume ($cm^3 \cdot g^{-1}$)	Average Pore Size (nm)
RGO	134.31	0.029	3.402
$SnIn_4S_8$	23.35	0.11	19.067
1% RGO/$SnIn_4S_8$	35.02	0.175	20.015
5% RGO/$SnIn_4S_8$	35.29	0.159	18.094
10% RGO/$SnIn_4S_8$	23.48	0.109	18.628

2.5. Optical Properties

Figure 5 shows the UV-Visible diffuse reflectance spectroscopy of pure $SnIn_4S_8$ and RGO/$SnIn_4S_8$ composites. Compared with pure $SnIn_4S_8$, the absorption of the RGO/$SnIn_4S_8$ composites obviously enhanced in ultraviolet (UV) and visible-light regions. Moreover, the absorption edge of the RGO/$SnIn_4S_8$ composites shows a red-shift to a higher wavelength, which is probably attributed to reduced reflection of light and the interfacial interaction between $SnIn_4S_8$ and RGO support to create a smooth charge–carrier transport [40].

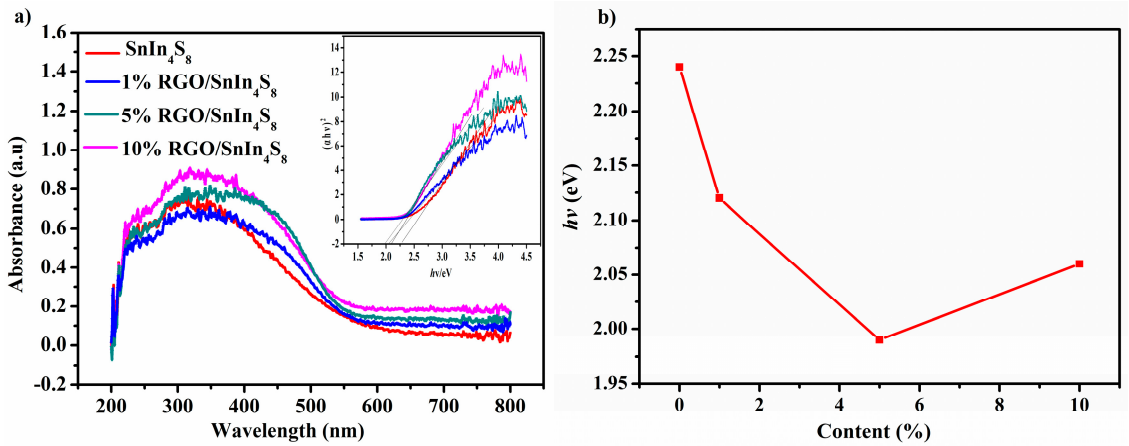

Figure 5. (**a**) UV-Visible diffuse reflectance spectra and plots of $(\alpha hv)^2$ versus hv (inset) of pure $SnIn_4S_8$ and RGO/$SnIn_4S_8$ composites with different RGO proportions; (**b**) the band gap can be changed with different RGO content in RGO/$SnIn_4S_8$ composites.

The band gap energies (E_g) can be estimated from the following Kubelka−Munk equation:

$$(\alpha hv)^n = k\left(hv - E_g\right)$$

where α is the absorption coefficient, k is a constant, hv is the photonic energy, E_g is the absorption band gap energy, n is 2 and 1/2 for a direct and indirect band gap semiconductor, respectively. Plot of $(\alpha hv)^2$ against hv based on the direct transition is shown in inset of Figure 5. According to the inset of Figure 5, the E_g of pure $SnIn_4S_8$, 1% RGO/$SnIn_4S_8$, 5% RGO/$SnIn_4S_8$ and 10% RGO/$SnIn_4S_8$ are estimated to be about 2.24, 2.12, 1.99 and 2.06 eV, respectively.

2.6. Mott-Schottky Analysis

The flat band potential (E_{fb}) of pure $SnIn_4S_8$ and RGO/$SnIn_4S_8$ composite can be estimated from the Mott-Schottky equation:

$$\frac{1}{C^2} = \frac{2}{\varepsilon\varepsilon_0 N_d}(E - E_{fb} - \frac{k_B T}{e})$$

where C is the space charge capacitance, ε is the dielectric constant of the semiconductor, ε_0 is the permittivity of free space, N_d is the donor density, E is the applied potential, E_{fb} is the flat-band potential, k_B is Boltzmann's constant (1.38×10^{-23} J·K^{-1}), T is the absolute temperature, and e is the electronic charge. The positive slope of the linear part indicates that pure $SnIn_4S_8$ and RGO/$SnIn_4S_8$ composite show the characteristic of n-type semiconductor (Figure 6). The E_{fb} value can be determined by extrapolating the linear part of the curve to $\frac{1}{C^2} = 0$, and the E_{fb} values of $SnIn_4S_8$ and RGO/$SnIn_4S_8$ composite are −0.614 and −0.294 V versus the saturated calomel electrode (SCE), respectively. Supposing the difference between flat potential and conduction band can be negligible for n-type semiconductors [41], the E_{fb} value is approximately equal to the E_{CB} value. Compared with pure $SnIn_4S_8$, the E_{CB} value of RGO/$SnIn_4S_8$ shifted to the positive direction, which could explain their enhanced photocatalytic activities. The electronic properties of pure $SnIn_4S_8$ and RGO/$SnIn_4S_8$ composite are listed in Table 2.

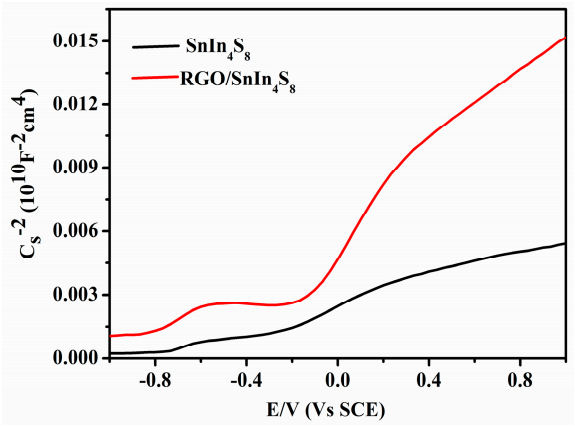

Figure 6. Mott–Schottky curves of pure $SnIn_4S_8$ and RGO/$SnIn_4S_8$ composites.

Table 2. Electronic properties of $SnIn_4S_8$ and RGO/$SnIn_4S_8$.

Sample	*Eg* (eV)	V_{fb} (V vs. SCE)	$V_{fb} \approx E_{CB}$ (V vs. NHE)	E_{VB} (V) [a]
$SnIn_4S_8$	2.24	−0.614	−0.372	1.868
5% RGO/$SnIn_4S_8$	1.99	−0.294	−0.052	1.938

[a] Calculated according to: $E_{VB} = E_g + E_{CB}$.

2.7. PL Emission Spectra

Figure 7 shows PL emission spectra of pure $SnIn_4S_8$ and RGO/$SnIn_4S_8$ composites with different RGO proportions. As displayed in Figure 7, with increasing RGO content from 0% to 5%, the PL intensity decreased, but further increasing RGO content from 5% to 10% resulted in the increase of PL signals. It can be seen that 5% RGO/$SnIn_4S_8$ composites gives the weakest PL intensity than that of all other samples. The results indicated that proper RGO content is able to retard the recombination of photogenerated electron–hole pairs more effectively, but excess RGO can promote the recombination of photogenerated electron–hole pairs.

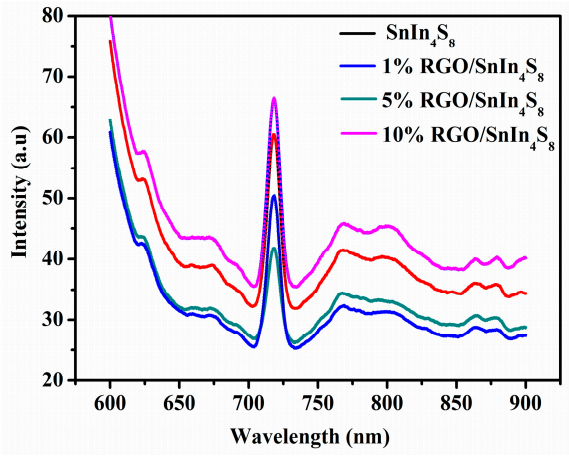

Figure 7. Photoluminescence (PL) spectra of pure $SnIn_4S_8$ and RGO /$SnIn_4S_8$ with different RGO content.

2.8. Adsorption Kinetics

Adsorption kinetics of pollutant molecules on photocatalysts is a key factor that could have an important influence on subsequent photocatalytic reaction. The adsorption kinetics of RhB on RGO, pure $SnIn_4S_8$ and RGO/$SnIn_4S_8$ composites with different RGO content was investigated in the dark, and the results are shown in Figure 8a. The adsorption amount of RhB on RGO, $SnIn_4S_8$ and RGO/$SnIn_4S_8$ increases rapidly with time during the first 15 min, then it increases slowly from 15 to 40 min, and finally it does not change, indicating that the adsorption/desorption equilibrium is established in 40 min. The equilibrium adsorption capacity of RGO, pure $SnIn_4S_8$ and RGO/$SnIn_4S_8$ composites with different RGO content based on experiment ($q_{e,exp}$) is listed in Table 3.

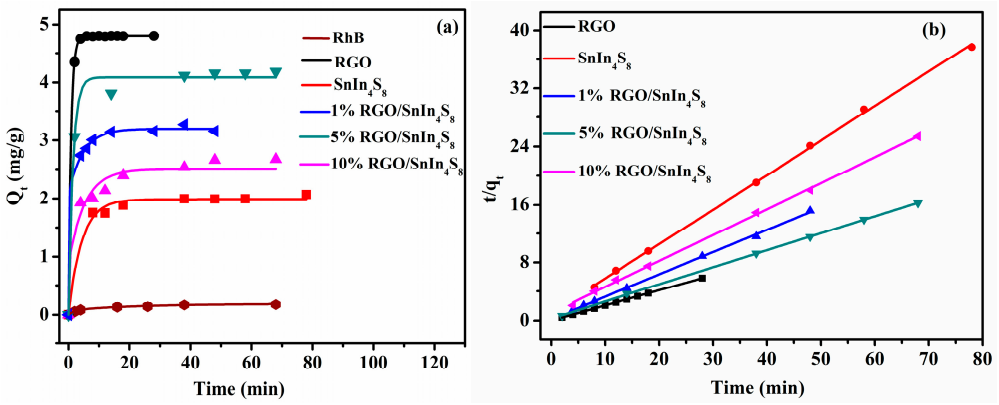

Figure 8. (**a**) adsorption kinetics for RhB adsorption on RGO, pure $SnIn_4S_8$, and RGO/$SnIn_4S_8$ composites with different RGO content; (**b**) linear plot of t/q vs. t for RGO, pure $SnIn_4S_8$, and RGO/$SnIn_4S_8$ composites with different RGO content.

Table 3. Adsorption kinetic parameters for RhB adsorption on RGO, pure $SnIn_4S_8$ and RGO/$SnIn_4S_8$ composites with different RGO content.

Sample	q_{exp} (mg·g^{-1})	Pseudo-First-Order			Pseudo-Second-Order		
		q_{cal} (mg·g^{-1})	K_1 (min^{-1})	R_2	q_{cal} (mg·g^{-1})	K_2 (g·mg^{-1}·min^{-1})	R_2
RGO	4.805	0.453	0.323	0.518	4.826	2.452	0.999
$SnIn_4S_8$	2.037	0.719	0.0476	0.712	2.102	0.218	0.999
1% RGO/$SnIn_4S_8$	3.157	2.837	0.3945	0.985	3.244	0.501	0.998
5% RGO/$SnIn_4S_8$	4.181	1.855	0.0818	0.919	4.243	0.208	0.999
10% RGO/$SnIn_4S_8$	2.677	1.690	0.0923	0.883	2.789	0.124	0.998

The pseudo-first-order and pseudo-second-order equations were used to fit the adsorption kinetics data of RhB on RGO, pure $SnIn_4S_8$ and RGO/$SnIn_4S_8$ composites. The pseudo-first-order rate equation is expressed as

$$ln\,(q_e - q_t) = -K_1 t + lnq_e$$

where q_e and q_t are the amounts of RhB adsorbed on photocatalysts at adsorption equilibrium and any time t, respectively (mg·g^{-1}); K_1 is adsorption rate constant (min^{-1}). The K_1, correlation coefficients (R^2) and calculated q_e ($q_{e,cal}$) values established from pseudo-first-order equation are depicted in Table 3. The R^2 values are relatively low, and the calculated $q_{e,cal}$ value is far from the experimental value ($q_{e,exp}$), indicating that the adsorption dynamics of RhB on RGO, pure $SnIn_4S_8$ and RGO/$SnIn_4S_8$ composites do not follow the pseudo-first-order kinetic model.

The linear form of pseudo-second-order model is expressed as followed:

$$\frac{t}{q_t} = \frac{t}{q_e} + \frac{1}{K_2 q_e^2}$$

where q_t and q_e is the amount of adsorbate at any time t and adsorption equilibrium (mg·g^{-1}), and K_2 is the constant rate of pseudo-second-order adsorption (g·mg^{-1}·min^{-1}). The regression curve of t/q_t versus t was rather linear (Figure 8b), and all parameters determined from pseudo-second-order model are also summarized in Table 3. The R^2 values are close to 1, and the calculated q_e ($q_{e,cal}$) from the pseudo-second-order model is very close to the experimental value, suggesting that RhB adsorption on RGO, pure $SnIn_4S_8$ and RGO/$SnIn_4S_8$ composites followed the pseudo-second-order model with an important chemisorption process.

2.9. Photocatalytic Activities

2.9.1. The Temporal Change of UV-Visible Spectra during the Photocatalytic Degradation

Figure 9 shows the UV-Visible spectral changes during the photocatalytic degradation of RhB under visible-light irradiation. As the reaction proceeds, the maximum absorption wavelength of RhB at 554 nm disappear quickly, and there are obvious hypsochromic shifts in the maximum absorption peak position, which shifts from 554 to 510 nm [42]. Moreover, the absorption intensity decreases. The inset shows the maximum absorption wavelength as a function of reaction time. During the early stage of photocatalytic degradation process, the peak positions did not change obviously because of the relatively high concentration of RhB and the low concentration of intermediate products. With a further degradation of RhB and the formation of abundant *N*-deethylated intermediate products, the blue-shift phenomenon became clear.

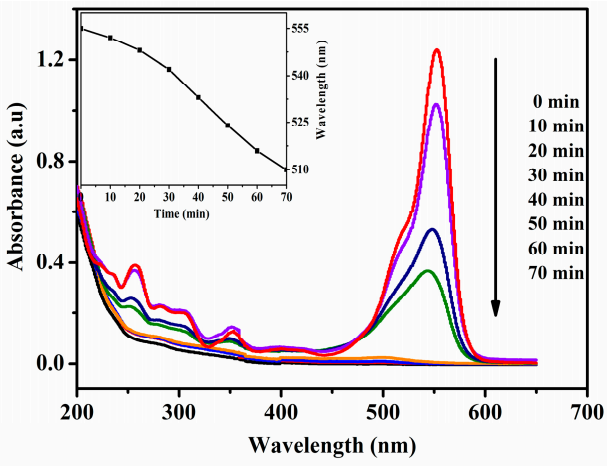

Figure 9. UV-Visible spectral changes of RhB solution in the presence of 5% RGO/$SnIn_4S_8$ as a function of reaction time. Inset: maximum absorption wavelength shifts as a function of reaction time.

2.9.2. Adsorption and Photocatalytic Degradation of RhB

In order to separate the contribution of adsorption and degradation in the experiment, the adsorption process in the dark and photocatalytic degradation of RhB over RGO, pure $SnIn_4S_8$ and RGO/$SnIn_4S_8$ composites under visible-light irradiation were carried out (Figure 10a). In the absence of a catalyst, the concentration change of RhB solution is very slight (around 6% during 70 min exposure), indicating that the self-degradation under visible-light irradiation can be neglected. In the presence of RGO, about 90% of RhB was adsorbed by RGO before the photodegradation, indicating that RGO is an excellent adsorbent. By discounting the adsorption contribution, the photocatalytic degradation of RhB over RGO, pure $SnIn_4S_8$ and RGO/$SnIn_4S_8$ composites under visible-light irradiation was shown in Figure 10b. In the presence of pure $SnIn_4S_8$ and RGO/$SnIn_4S_8$ composites, RhB photodegradation is remarkably enhanced. The photocatalytic activity of RGO/$SnIn_4S_8$ composite is much higher than that of pure $SnIn_4S_8$ and RGO, and the photocatalytic activity of RGO/$SnIn_4S_8$ composites is greatly influenced by the RGO content. The photocatalytic activity of RGO/$SnIn_4S_8$ composite increases with increasing RGO content from 0% to 5%. When the percent of RGO reaches 5%, RGO/$SnIn_4S_8$ exhibits the highest photocatalytic activity, giving rise to the almost complete removal of RhB within 70 min under visible-light irradiation. However, as the proportion of RGO further increases, the degradation efficiency decreases gradually, and the degradation of RhB needs much longer time. One possible reason is that an appropriate amount of RGO is beneficial for the generation and transfer of photo-generated electrons and holes at heterojunction interfaces, while excessive RGO could shield $SnIn_4S_8$ from light as well as promote electron–hole recombination [43]. Therefore, due to the demands of both the charge transfer and light harvesting, the photocatalytic activity of RGO/$SnIn_4S_8$ first increases and then decreases with the increase of RGO content, leading to the highest photocatalytic activity of 5% RGO/$SnIn_4S_8$.

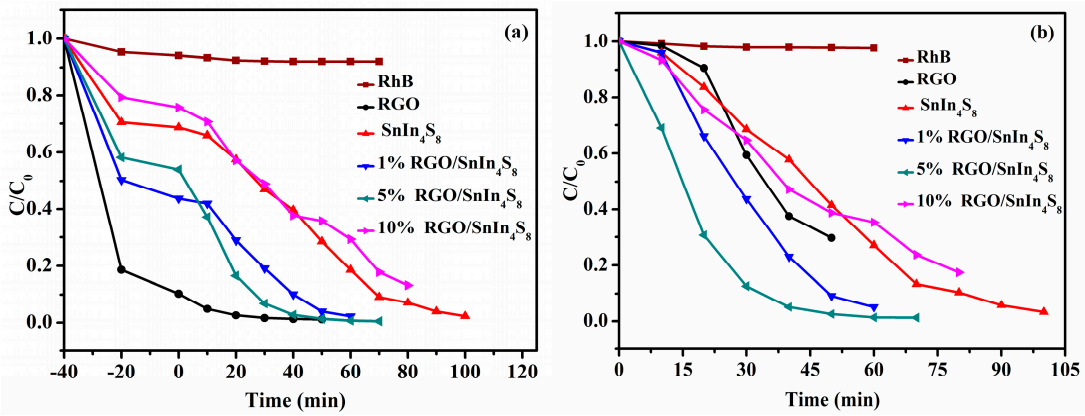

Figure 10. Photodegradation of RhB over RGO, pure $SnIn_4S_8$ and RGO/$SnIn_4S_8$ composites with different RGO content under visible-light irradiation: (**a**) including the dark adsorption; (**b**) discounting the adsorption contribution.

2.9.3. Mineralization of Aqueous RhB

The mineralization efficiency of RhB was monitored by TOC analyzer. Figure 11 shows TOC removal of RhB in presence of RGO/$SnIn_4S_8$ under visible-light irradiation for 160 min. The TOC removal efficiency was calculated according to the following equation:

$$TOC\ removal\ efficiency = \frac{TOC_0 - TOC_t}{TOC_0} \times 100\%$$

where TOC_0 represents the initial TOC value of RhB solution, and TOC_t is the TOC value at any time t. It can be seen from Figure 11 that TOC removal efficiency of RhB solution increases with increasing visible-light irradiation time, and the TOC removal efficiency reaches 73.17% after exposure to visible-light irradiation for 160 min, indicating that the most of RhB and its *N*-deethylation intermediate products were decomposed into inorganic species.

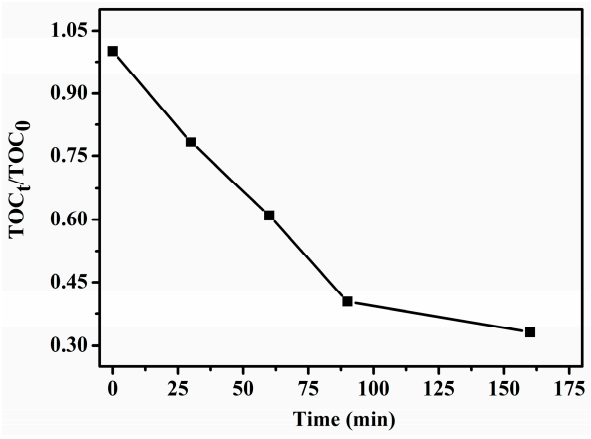

Figure 11. Total organic carbon (TOC) changes of aqueous RhB on 5% RGO/$SnIn_4S_8$ under visible-light irradiation.

2.10. Separation and Identification of Intermediates

To further understand the photocatalytic degradation and mineralization pathways of RhB, RhB and its intermediate products were analyzed using HPLC-MS (Figure 12). According to the m/z values of the intermediate products and the structure of RhB, we have inferred the pathways of photocatalytic degradation and mineralization (Figure 13). The mass peaks at m/z 443, 413, 399, 346,

and 328 correspond to RhB and its *N*-deethylated intermediates (*N*,*N*-diethyl-*N*'-ethylrhodamine (DER), *N*,*N*-diethylrhodamine (DR), *N*-ethylrhodamine (ER), and rhodamine (R)). As further oxidation proceeded, adipic acid, phthalic acid, isophthalic acid, and terephthalic acid were generated. Finally, these small molecules were mineralized into CO_2 and H_2O, which can be proved by TOC results.

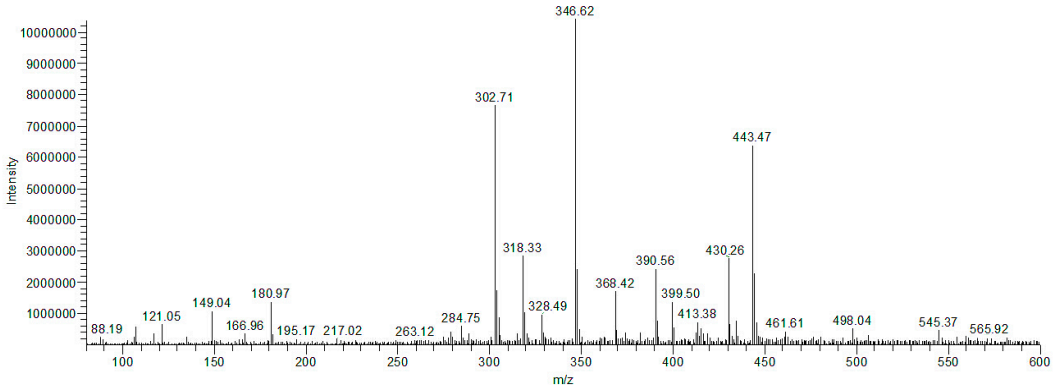

Figure 12. Mass spectrum view of RhB and its intermediates that appeared in the photodegradation process.

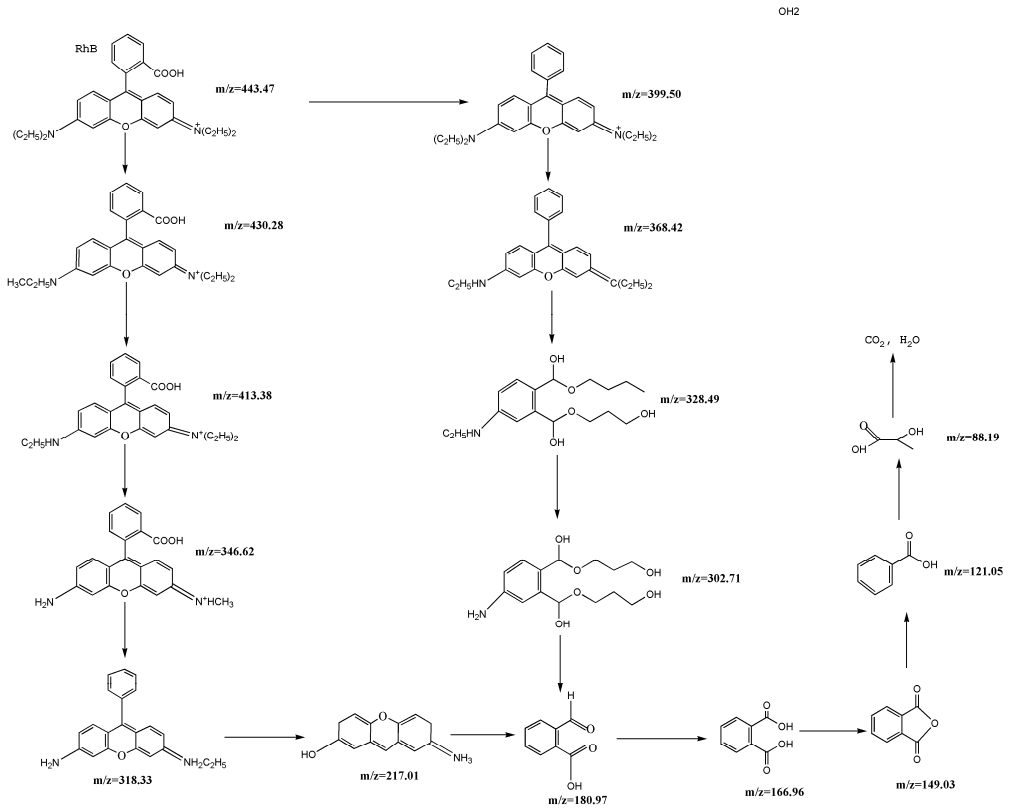

Figure 13. The proposed degradation pathways of RhB in RGO/$SnIn_4S_8$ suspension under visible-light irradiation.

2.11. Photocatalytic Mechanism

It is very important to examine main reactive species (such as h^+, ·OH and $\cdot O_2^-$ radicals) in photocatalytic reaction for understanding the photocatalytic mechanism of RGO/$SnIn_4S_8$ under visible-light irradiation. Figure 14 shows the degradation efficiency of RhB over 5% RGO/$SnIn_4S_8$ in the presence of isopropanol (IPA, ·OH quencher), triethanolamine (TEOA, h^+ quencher) and benzoquinone (BQ, $\cdot O_2^-$ quencher). When no quenchers were added, the degradation efficiency of RhB is 98.72%.

When TEOA and BQ scavengers were added, the RhB degradation efficiency was significantly reduced to 6.57% and 33.40%, respectively. In the case of adding an IPA scavenger, the degradation efficiency of RhB decreased to 68.30%. Therefore, it can be concluded that h^+, $\cdot O_2^-$ and ·OH are the main active species which play crucial roles in the degradation of RhB, and the order of affecting degradation efficiency of RhB follows that of $h^+ > \cdot O_2^- >$ ·OH.

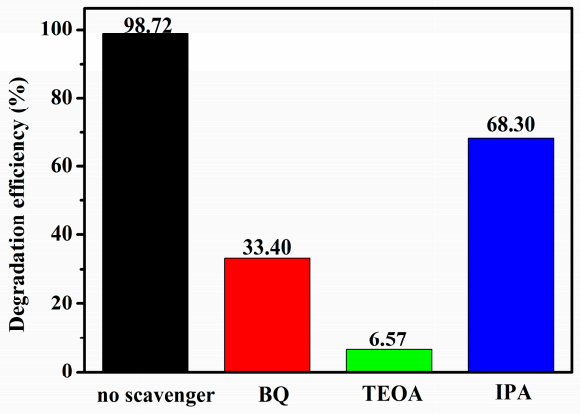

Figure 14. Effect of different scavengers on the RhB photodegradation by 5% RGO/$SnIn_4S_8$ under visible-light irradiation for 120 min.

Based on the experiment results and the reported literature [44–46], the generation and transfer of the photogenerated electrons and holes in RGO/$SnIn_4S_8$ composites are illustrated in Scheme 1. As shown in Scheme 1, under visible-light irradiation, the electrons (e^-) excited in valence band (VB) would transfer to the conduction band (CB) of $SnIn_4S_8$, whereas the holes (h^+) would generate in the VB of $SnIn_4S_8$. The photo-generated e^- in the CB of the $SnIn_4S_8$ can be injected into RGO, therefore hindering the recombination process of the e^--h^+ pairs. The photo-generated e^- in RGO could react with adsorbed O_2 to form $\cdot O_2^-$ radicals. Most of $\cdot O_2^-$ radicals play an important role in the degradation of RhB molecules, others could further react with H_2O to generate hydroxyl radicals (·OH). The h^+ in the VB of $SnIn_4S_8$ are decisive to oxidize RhB molecules adsorbed on the surface of RGO/$SnIn_4S_8$ composites, meanwhile, $\cdot O_2^-$ and ·OH radicals are beneficial to the degradation of RhB. The photocatalytic process of RhB under visible-light irradiation, among with ^{1}RhB* and ^{3}RhB* represent the ö$_{ST}$ and the triplet respectively [47,48]. The equations are as follows:

$$e^- + RGO \rightarrow RGO(e^-) \quad (1)$$

$$RGO(e^-) + O_2 \rightarrow \bullet O_2^- \quad (2)$$

$$\bullet O_2^- + H_2O \rightarrow \bullet O_2H + OH^- \quad (3)$$

$$RhB^+\bullet + \bullet O_2 \rightarrow RhBO_2 \rightarrow \text{decomposition products} \quad (4)$$

$$RhB^+ + HO_2\bullet \rightarrow \text{decomposition products} \quad (5)$$

Equation (2) is followed by Reaction (7) and the following sequence:

$$RhB + hv(vis) \rightarrow {}^1RhB^* \; or \; {}^3RhB^3 \quad (6)$$

$${}^1RhB^* \; or \; {}^3RhB^* + RGO/SnIn_4S_8 \rightarrow RhB^+\bullet + SnIn_4S_8(h^+ + e^-) \quad (7)$$

$$RhB^+\bullet \rightarrow \text{decomposition products} \quad (8)$$

$$RhB^+\bullet + OH^- \rightarrow RhB + \bullet OH \quad (9)$$

$$RhB + \bullet OH \rightarrow \text{decomposition products} \quad (10)$$

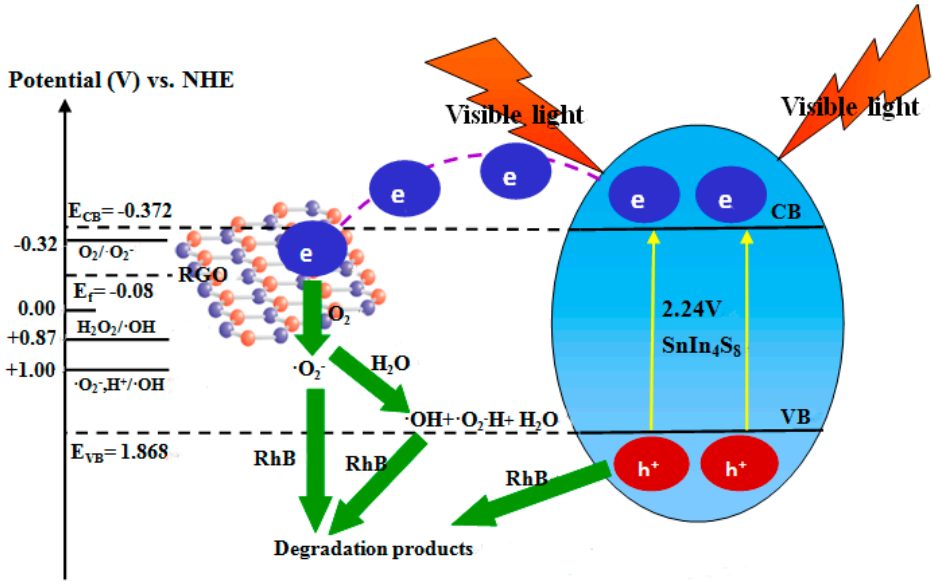

Scheme 1. A schematic illustration for the photocatalytic mechanism of RhB on reduced graphene oxide (RGO)/$SnIn_4S_8$ composites under visible-light irradiation.

2.12. Regeneration and Reuse of Spent RGO/$SnIn_4S_8$ Composites

The stability of RGO/$SnIn_4S_8$ composites has also been studied to evaluate its economic value and practical application. As shown in Figure 15, after four consecutive photocatalytic degradation-regeneration cycles, the photocatalytic performance of the regenerated 5% RGO/$SnIn_4S_8$ composites is similar to that of their fresh counterparts, indicating that 5% RGO/$SnIn_4S_8$ composites exhibit high stability, and could be used repeatedly.

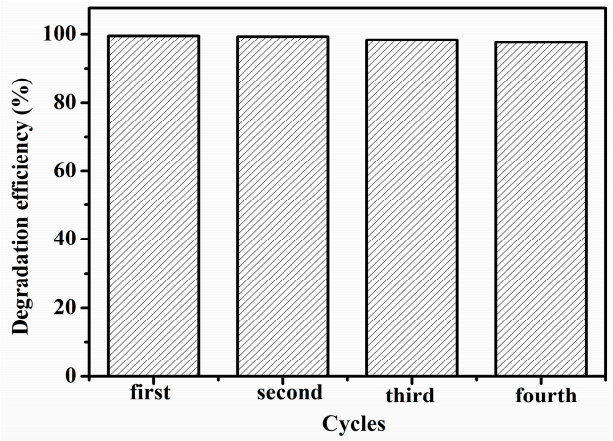

Figure 15. Regeneration and reuse of 5% RGO/$SnIn_4S_8$ composites.

3. Experimental Section

3.1. Materials and Chemicals

Thioacetamide (TAA) was attained from Tianjin Chemical Reagent Plant (Tianjin, China). Tin (IV) chloride pentahydrate ($SnCl_4 \cdot 5H_2O$) and indium (III) chloride tetrahydrate ($InCl_3 \cdot 4H_2O$) were received from Aladdin Chemistry Co. Ltd. (Shanghai, China). Graphite powder, 80% hydrazine hydrate, anhydrous ethanol, sodium sulfate (Na_2SO_4) and *iso*-propyl alcohol (IPA) were obtained from Shantou Xilong Chemical Co., Ltd. (Shantou, China). *p*-Benzoquinone (BQ) was supplied by Shanghai Crystal

Pure Reagent Co., Ltd. (Shanghai, China). Triethanolamine (TEOA) was acquired from Shanghai Chemical Reagent Co., Ltd. (Shanghai, China). Rhodamine B (RhB) was provided by Shanghai Chemical Technology Co., Ltd. (Shanghai, China). All the reagents were of analytical grade and used without further purification. Deionized water was further purified using a Milli-Q water system (Bedford, MD, USA).

3.2. The Low-Temperature Co-Precipitation Synthesis of Pure $SnIn_4S_8$ and RGO/$SnIn_4S_8$ Composite

Graphene oxide (GO) was prepared by the modified Hummers method [49], and then GO was reduced to RGO by 80% hydrazine hydrate. To synthesize RGO/$SnIn_4S_8$ composites with different amount of RGO, a simple low-temperature co-precipitation method was used. In a typical procedure, 0.521 g of $SnCl_4{\cdot}5H_2O$ (2.0 mmol) and 1.769 g of $InCl_3{\cdot}4H_2O$ (8.0 mmol) were dissolved in 50 mL of anhydrous ethanol under magnetic stirring, and then 1.127 g of TAA (15 mmol) was added to the above solution. The mixture solution was stirred for about 25 min until the solution became transparent, then a certain amount of RGO was added to the mixture solution and followed by ultrasonication for 20 min to form a transparent solution. The above solution was transferred to a 150 mL three flask with a condensing unit and maintained at bath temperature of 80 °C for 5 h under continuous stirring, then cooled to room temperature naturally. The obtained yellow precipitate was filtered and washed with distilled water and absolute ethanol several times, and dried at 80 °C in vacuum for 12 h. The samples with different molar ratio of C to Sn were designated as pure $SnIn_4S_8$, 1% RGO/$SnIn_4S_8$, 5% RGO/$SnIn_4S_8$ and 10% RGO/$SnIn_4S_8$, respectively.

3.3. Characterization

U-3900H scan UV-Vis spectrophotometer (Hitachi, Tokyo, Japan) equipped with a Labsphere diffuse reflectance accessory was used to obtain the reflectance spectra of the photocatalysts over a range of 200–800 nm. Morphologies of the photocatalysts were analyzed by scanning electron microscopy (SEM) instrument (Shimadzu, Kyoto, Japan). BET surface areas and pore structures were measured using a GEMINI VII 2390 surface area and porosity analyzer (Micromeritics, Atlanta, GA, USA). X-ray diffraction (XRD) patterns of products were obtained by using an automatic X-ray diffractometer (XRD, Rigaku D/max 2200PC, Karlsruhe, Germany) with Cu Kα radiation. Raman spectra of samples were obtained using a LabRAM HR spectrophotometer (Jobin Yvon, Paris, France) with an excitation wavelength of 632.8 nm. The photoluminescence (PL) were measured using F-7000 fluorescence spectrophotometer (Hitachi, Tokyo, Japan) with an excitation wavelength of 474 nm. The total organic carbon (TOC) of the samples was analyzed by using an Apollo 9000 TOC analyzer (Terkmar-Dohrmann, Atlanta, GA, USA). The intermediate products were analyzed by using LCQ-Deca-XP high performance liquid chromatography-tandem mass spectrometry (HPLC-MS, Thermo Finnigan, Atlanta, GA, USA).

3.4. Electrochemical Measurement

The flat-band potential of 5% RGO/$SnIn_4S_8$ was determined by extrapolating the Mott-Schottky plots. Mott-Schottky plots were performed on an electrochemical workstation (CHI660C, Shanghai Chenhua Instrument Corporation, Beijing, China) with a standard three-electrode cell in the potential range between −1.0 and 1.0 V with scan frequency of 1000 Hz and 0.025 V sinus amplitude. This three-electrode cell was consisted of a saturated calomel electrode (SCE) as reference electrode, a graphite electrode as counter electrode, RGO/$SnIn_4S_8$-modified indium tin oxide (ITO) conducting glass as the working electrode, and 0.5 $mol{\cdot}L^{-1}$ Na_2SO_4 as the electrolyte.

3.5. Adsorption Dynamics in the Dark

In addition, 0.03 g of pure $SnIn_4S_8$, 1% RGO/$SnIn_4S_8$, 5% RGO/$SnIn_4S_8$, 10% RGO/$SnIn_4S_8$, or RGO was mixed with 160 mL of 10 $mg{\cdot}L^{-1}$ RhB solution in a conical flask, respectively. The conical flasks were shaken at 20 °C in the dark. In addition, 3 mL suspension was sampled at different time

intervals, and filtered immediately to remove the photocatalysts. The concentration of RhB in the filtrate was measured by HPLC with detection wavelength of 553.5 nm. The adsorbed amount at any time t (q_t) is calculated as follows:

$$q_t = \frac{(C_0 - C_t)V}{m}$$

where C_0 (mg·L^{-1}) is the initial RhB concentration, C_t (mg·L^{-1}) is the RhB concentration at time t, V (mL) is the volume of RhB solution, and m (g) is the mass of the photocatalysts.

3.6. Visible-Light Photocatalytic Activity Measurement

A 300 W xenon lamp (PLS-SXE300, Beijing Trusttech Co., Ltd., Beijing, China) with a 400 nm cut-off filter (400 nm < λ < 780 nm) was used as the source of visible light. The photocatalytic activities of pure $SnIn_4S_8$ and RGO/$SnIn_4S_8$ were evaluated by the degradation of RhB under visible-light irradiation. Typically, 30 mg of pure $SnIn_4S_8$ or RGO/$SnIn_4S_8$ composite was added to 160 mL of RhB solution (10 mg·L^{-1}), respectively. Before irradiation, the suspensions were magnetically stirred in the dark for 40 min in order to establish an adsorption-desorption equilibrium. Under continuous stirring, the mixed solution was irradiated by visible light. The reaction suspension was sampled at intervals of 10 min. After immediate filtration, the clear solution was analyzed using a 754 UV-Vis spectrometer at a wavelength of 553.5 nm, which is the maximum absorption wavelength of RhB. The concentration of RhB was estimated by a calibration curve. The intermediate products were analyzed by using HPLC-MS.

3.7. Regeneration and Reuse of Spent RGO/$SnIn_4S_8$ Composite Catalyst

In order to evaluate the stability and reusability of RGO/$SnIn_4S_8$, consecutive photocatalytic degradation-regeneration cycles were repeated four times. The spent RGO/$SnIn_4S_8$ composite was recovered from the mixture solution by filtration and washed with plenty of water (0.1 g RGO/$SnIn_4S_8$ composite with 400 mL water), then dried at 60 °C for 4 h. The regenerated RGO/$SnIn_4S_8$ composite was used for subsequent cycles of photocatalytic degradation under similar reaction conditions as carried out with fresh catalyst.

4. Conclusions

We successfully prepared hierarchically porous reduced graphene oxide/$SnIn_4S_8$ (RGO/$SnIn_4S_8$) composites with visible-light response and strong mineralization ability by a facile low-temperature co-precipitation method. Compared with pure $SnIn_4S_8$, RGO/$SnIn_4S_8$ composite exhibits enhanced absorption in UV and visible-light range. The RGO content was optimized, and the optimal content of RGO nanosheets is 5%. The optimal 5% RGO/$SnIn_4S_8$ possesses the best photocatalytic degradation efficiency and mineralization performance with complete degradation of Rhodamine B within 70 min and 73.17% mineralization yield within 160 min under visible-light irradiation, which is much higher than that of pure $SnIn_4S_8$. The main reactive species that affect degradation and mineralization efficiency of RhB follow the order of $h^+ > \cdot O_2^- > \cdot OH$. The intermediate products of RhB degradation were analyzed, and the possible degradation pathways and detailed degradation mechanism were proposed. Moreover, 5% RGO/$SnIn_4S_8$ exhibits excellent reusability and stability without obvious decrease of photocatalytic activity.

Acknowledgments: This work was supported by Natural Science Foundation of China (51308278, 51178213, 51238002), National Science Fund for Excellent Young Scholars (51422807), Department of Education Fund of Jiangxi Province (GJJ150742) and Science Fund for Excellent Young Scholars of Jiangxi Province (20122BAB213014).

Author Contributions: Fang Deng conceived and designed the experiments; Xule Pei performed the experiments; Fang Deng and Xule Pei analyzed the data; Key Laboratory of Jiangxi Province for Persistent Pollutants Control and Resources Recycle, Nanchang Hangkong University contributed reagents/materials/analysis tools; All the authors discussed the results, analyzed data and wrote this paper.

Conflicts of Interest: The authors declare no conflict of interests.

References

1. Elimelech, M.; Phillip, W.A. The future of seawater desalination: Energy, technology, and the environment. *Science* **2011**, *333*, 712–717. [CrossRef] [PubMed]
2. Chao, J.; Xie, Z.; Duan, X.B.; Dong, Y.; Wang, Z.; Xu, J.; Liang, B.; Shan, B.; Ye, J.; Chen, D.; et al. Visible-light-driven photocatalytic and photoelectrochemical properties of porous SnS_x(x = 1,2) architectures. *CrystEngComm.* **2012**, *14*, 3163–3168. [CrossRef]
3. Elfghi, F.M.; Zaidi, S.A.; Abdullah, E.C.; Ali, K.M. Applications of graphene and its derivatives as an adsorbent for heavy metal and dye removal: A systematic and comprehensive overview. *RSC Adv.* **2015**, *5*, 50392–50420.
4. Marahel, F.; Khan, M.A.; Marahelac, E.; Bayestiac, I.; Desalin, S. Kinetics, thermodynamics, and isotherm studies for the adsorption of BR2 dye onto avocado integument. *Water Treat.* **2015**, *53*, 826–835. [CrossRef]
5. Zhang, X.; Chen, C.; Lin, P.; Hou, A.; Niu, Z.; Wang, J. Emergency drinking water treatment during source water pollution accidents in China: Origin analysis, framework and technologies. *Environ. Sci. Technol.* **2011**, *45*, 161–167. [CrossRef] [PubMed]
6. Xiong, Z.; Zhang, L.L.; Ma, J.Z.; Zhao, X.S. Photocatalytic degration of dyes over graphene-gold nanocomposites under visible light irradiation. *Chem. Commun.* **2010**, *46*, 6099–6101. [CrossRef] [PubMed]
7. Lei, Y.; Xing, Y.; Fan, W.; Song, S.; Zhang, H. Synthesis characterization and optical property of flower-like indium tin sulfide nanostructures. *Dalton Trans.* **2009**, *162*, 1620–1623. [CrossRef] [PubMed]
8. Ge, M.; Zhu, N.; Zhao, Y.; Li, J.; Liu, L. Sunlight-assisted degradation of dye pollutants in Ag_3PO_4 suspension. *Ind. Eng.Chem. Res.* **2012**, *51*, 5167–5173. [CrossRef]
9. Wang, J.Q.; Liu, Y.H.; Chen, M.W. Excellent capability in degrading azo dyes by MgZn-based metallic glass powders. *Nature* **2012**, *2*, 148–152. [CrossRef] [PubMed]
10. Dukkancl, M.; Vinatoru, M.; Mason, T.J. The sonochemical decolourisation of textile azo dye Orange II: Effects of Fenton type reagents and UV light. *Ultrason. Sonochem.* **2014**, *21*, 846–853. [CrossRef] [PubMed]
11. Gu, Y.; Zhang, Y.; Zhang, F.; Wei, J.; Wang, C.; Du, Y.; Ye, W. Investigation of photoelectrocatalytic activity of Cu_2O nanoparticles for *p*-nitrophenol using rotating ring-disk electrode and application for electrocatalytic determination. *Electrochim. Acta* **2010**, *56*, 953–958. [CrossRef]
12. Cheng, Z.; Liao, J.; He, B.; Zhang, F.; Zhang, F.; Huang, X.; Zhou, L. One-Step fabrication of graphene oxide enhanced magnetic composite gel for highly efficient dye adsorption and catalysis. *ACS Sustain. Chem. Eng.* **2015**, *3*, 1677–1685. [CrossRef]
13. Mondal, T.; Bhowmick, A.K. Synthesis and characterization of bi-functionalized graphene and expanded graphite using *n*-butyl lithium and their use for efficient water soluble dye adsorption. *J. Mater. Chem. A* **2013**, *1*, 8144–8153. [CrossRef]
14. Zhou, L.; He, B.; Huang, J. One-step synthesis of robust amine-and vinyl-capped magnetic iron oxide nanoparticles for polymer grafting, dye adsorption, and catalysis. *ACS Appl. Mater. Inter.* **2013**, *5*, 8678–8685. [CrossRef] [PubMed]
15. Yang, Y.; Liao, H.; Tong, Z.; Wang, C. Porous Ag/polymer composite microspheres for adsorption and catalytic degradation of organic dyes in aqueous solutions. *Compos. Sci. Technol.* **2015**, *107*, 137–144. [CrossRef]
16. Nishikawa, M.; Mitani, Y.; Nosaka, Y. Photocatalytic reaction mechanism of Fe(III)-grafted TiO_2 studied by means of ESR spectroscopy and chemi-luminescence photometry. *J. Phys. Chem. C* **2012**, *116*, 14900–14907. [CrossRef]
17. Dinh, C.T.; Yen, H.; Kleitz, F.; Do, T.O. Three-dimensional ordered assembly of thin-shell Au/TiO_2 hollow nanospheres for enhanced visible-light-driven photocatalysis. *Angew. Chem. Int. Ed.* **2014**, *53*, 6618–6623. [CrossRef] [PubMed]
18. Yu, J.; Ma, T.; Liu, G.; Cheng, B. Enhanced photocatalytic activity of bimodal meso-porous titania powders by C_{60} modification. *Dalton Trans.* **2011**, *40*, 6635–6644. [CrossRef] [PubMed]
19. Deng, F.; Liu, Y.; Luo, X.B.; Wu, S.L.; Luo, S.L.; Au, C.; Qi, R. Sol-hydrothermal synthesis of inorganic-framework molecularly imprinted TiO_2/SiO_2 nanocomposite and its preferential photocatalytic degradation towards target contaminant. *J. Hazard. Mater.* **2014**, *278*, 108–115.
20. Sackmann, E.K.; Fulton, A.; Beebe, D.J. The present and future role of microfluidics in biomedical research. *Nature* **2014**, *507*, 181–189. [CrossRef] [PubMed]

21. Liu, S.; Liu, C.; Wang, W.; Cheng, B.; Yu, J. Unique photocatalytic oxidation reactivity and selectivity of TiO_2-graphene nanocomposites. *Nanoscale* **2012**, *4*, 3193–3200. [PubMed]
22. Yang, X.; Chen, W.; Huang, J.; Zhou, Y.; Zhu, Y.; Li, C. Rapid degradation of methylene blue in a novel heterogeneous Fe_3O_4@rGO@TiO_2-catalyzed photo-Fenton system. *Nature* **2015**, *5*, 10632–10642. [CrossRef] [PubMed]
23. Niu, M.; Cheng, D.; Cao, D. SiH/TiO_2 and GeH/TiO_2 heterojunctions: Promising TiO_2-based photocatalysts under visible light. *Nature* **2014**, *4*, 4810–4815. [CrossRef] [PubMed]
24. Yan, T.; Li, L.; Li, G.; Wang, Y.; Hu, W.; Guan, X. Porous $SnIn_4S_8$ microspheres in a new polymorph that promotes dyes degradation under visible light irradiation. *J. Hazard. Mater.* **2011**, *186*, 272–279. [CrossRef] [PubMed]
25. Lei, Y.Q.; Wang, G.H.; Zhou, L.; Hu, W.; Song, S.Y.; Fan, W.Q.; Zhang, H.J. Cubic spinel In_4SnS_8: Electrical transport properties and electrochemical hydrogen storage properties. *Dalton Trans.* **2010**, *39*, 7021–7024. [CrossRef] [PubMed]
26. Wang, L.; Li, X.; Teng, W.; Zhao, Q.; Shi, Y.; Yue, R.; Chen, Y. Efficient photocatalytic reduction of aqueous Cr(VI) over flower-like $SnIn_4S_8$ microspheres under visible light illumination. *J. Hazard. Mater.* **2013**, *244–245*, 681–688. [CrossRef] [PubMed]
27. Chen, D.; Feng, H.; Li, J. Graphene oxide: Preparation, functionalization and electrochemical applications. *Chem. Rev.* **2012**, *112*, 6027–6053. [CrossRef] [PubMed]
28. Xiang, Q.; Yu, J.; Jaroniec, M. Graphene-based semiconductor photocatalysts. *Chem. Soc. Rev.* **2012**, *41*, 782–796. [CrossRef] [PubMed]
29. Tu, W.; Zhou, Y.; Zou, Z. Versatile graphene-promoting photocatalytic performance of semiconductors: Basic principles, synthesis, solar Energy Conversion, and environmental applications. *Adv. Funct. Mater.* **2013**, *23*, 4996–5008. [CrossRef]
30. Ong, W.L.; Gao, M.; Ho, G.W. Hybrid organic PVDF–inorganic M–rGO–TiO_2 (M = Ag, Pt) nanocomposites for multifunctional volatile organic compound sensing and photocatalytic degradation–H_2 production. *Nanoscale* **2013**, *5*, 11283–11290. [CrossRef] [PubMed]
31. Gao, M.; Peh, C.K.N.; Ong, W.L.; Ho, G.W. Green chemistry synthesis of a nanocomposite grapheme hydrogel with three-dimensional nano-mesopores for photocatalytic H_2 production. *RSC Adv.* **2013**, *3*, 13169–13177. [CrossRef]
32. Liu, X.; Pan, L.; Lv, T.; Zhu, G.; Sun, Z.; Sun, C. Microwave-assisted synthesis of CdS-reduced graphene oxide composites for photocatalytic reduction of Cr(VI). *Chem. Commun.* **2011**, *47*, 11984–11986. [CrossRef] [PubMed]
33. Yavari, F.; Kritzinger, C.; Gaire, C.; Song, L.; Gulapalli, H.; Tasciuc1, T.B.; Ajayan, P.M.; Koratkar, N. Tunable bandgap in graphene by the controlled adsorption of water molecules. *Small* **2010**, *6*, 2535–2538. [CrossRef] [PubMed]
34. Ding, M.Y.; Tang, Y.; Star, A. Understanding interfaces in metal–graphitic hybrid nanostructures. *J. Phys. Chem. Lett.* **2013**, *4*, 147–160. [CrossRef] [PubMed]
35. Perera, S.D.; Mariano, R.G.; Vu, K.; Nour, N.; Seitz, O.; Chabal, Y.; Balkus, K.J. Hydrothermal synthesis of graphene-TiO_2 nanotube composites with enhanced photocatalytic activity. *ACS Catal.* **2012**, *2*, 949–956. [CrossRef]
36. Leofanti, G.; Padovan, M.; Tozzola, G.; Venturelli, B. Surface area and pore texture of catalysts. *Catal. Today* **1998**, *90*, 207–219. [CrossRef]
37. Walton, K.S.; Snurr, R.Q. Applicability of the BET method for determining surface areas of microporous metal−organic frameworks. *J. Am. Chem. Soc.* **2007**, *129*, 8552–8556. [CrossRef] [PubMed]
38. Lozano-Castelló, D.; Cazorla-Amorós, D.; Linares-Solano, A.; Shiraishi, S.; Kurihara, H.; Oya, A. Influence of pore structure and surface chemistry on electric double layer capacitance in non-aqueous electrolyte. *Carbon* **2003**, *41*, 1765–1775. [CrossRef]
39. Xiang, Q.J.; Lv, K.L.; Yu, J.G. Pivotal role of fluorine in enhanced photocatalytic activity of anatase TiO_2 nanosheets with dominant (001) facets for the photocatalytic degradation of acetone in air. *Appl. Catal. B Environ.* **2010**, *96*, 557–564. [CrossRef]
40. Zhang, J.; Yu, J.; Jaroniec, M.; Gong, J.R. Noble metal-free reduced graphene oxide-$Zn_xCd_{1-x}S$ nanocomposite with enhanced solar photocatalytic H_2-production performance. *Nano Lett.* **2012**, *12*, 4584–4589. [CrossRef] [PubMed]

41. Lim, J.; Murugan, P.; Lakshminarasimhan, N.; Kim, J.Y.; Lee, J.S.; Lee, S.H.; Choi, W. Synergic photocatalytic effects of nitrogen and niobium co-doping in TiO_2 for the redox conversion of aquatic pollutants under visible light. *J. Catal.* **2014**, *310*, 91–99. [CrossRef]
42. Yang, Y.H.; Chen, X.Y.; Feng, Y.; Yang, G.W. Physical mechanism of blue-shift of UV luminescence of a single pencil-like ZnO nanowire. *Nano Lett.* **2007**, *7*, 3879–3883. [CrossRef] [PubMed]
43. Bu, Y.; Chen, Z.; Li, W.; Hou, B. Highly efficient photocatalytic performance of graphene−ZnO quasi-shell-core composite material. *ACS Appl. Mater. Inter.* **2013**, *5*, 12361–12368. [CrossRef] [PubMed]
44. Ong, W.; Voon, S.; Tan, L.; Goh, B.; Yong, S.; Chai, S. Enhanced daylight-induced photocatalytic activity of solvent exfoliated graphene (SEG)/ZnO hybrid nanocomposites toward degradation of reactive black 5. *Ind. Eng. Chem. Res.* **2014**, *53*, 17333–17344. [CrossRef]
45. Yang, L.; Sun, W.; Luo, S.; Luo, Y. White fungus-like mesoporous Bi_2S_3 ball/TiO_2 heterojunction with high photocatalytic efficiency in purifying 2,4-dichlorophenoxyaceticacid/Cr(VI) contaminated water. *Appl. Catal. B Environ.* **2014**, *156–157*, 25–34. [CrossRef]
46. Zhang, Y.; Chen, Z.; Liu, S.; Xu, Y. Size effect induced activity enhancement and anti-photocorrosion of reduced graphene oxide/ZnO composites for degradation of organic dyes and reduction of Cr(VI) in water. *Appl. Catal. B Environ.* **2013**, *140–141*, 598–607. [CrossRef]
47. Rajeshwar, K.; Osugi, M.E.; Chanmanee, W.; Chenthamarakshan, C.R.; Zanoni, M.V.B.; Kajitvichyanukul, P.; Krishnan-Ayer, R. Heterogeneous photocatalytic treatment of organic dyes in air and aqueous media. *J. Photoch. Photobio. C Photochem. Rev.* **2008**, *9*, 171–192. [CrossRef]
48. Qu, P.; Zhao, J.C.; Zang, L.; Shen, T.; Hidaka, H.S. Enhancement of the photoinduced electron transfer from cationic dyes to colloidal TiO_2 particles by addition of an anionic surfactant in acidic media. *Colloids Surfaces A Physicochem. Eng. Aspects* **1998**, *138*, 39–50. [CrossRef]
49. Avouris, P. Graphene: Electronic and photonic properties and devices. *Nano Lett.* **2010**, *10*, 4285–4294. [CrossRef] [PubMed]